J Solid State Electrochem (2011) 15:313–327
DOI 10.1007/s10008-010-1203-9

ORIGINAL PAPER

Transport, thermomechanical, and electrode properties of perovskite-type $(La_{0.75-x}Sr_{0.25+x})_{0.95}Mn_{0.5}Cr_{0.5-x}Ti_xO_{3-\delta}(x = 0-0.5)$

Vladislav A. Kolotygin · Ekaterina V. Tsipis · Aliaksandr L. Shaula · Eugene N. Naumovich · Jorge R. Frade · Sergey I. Bredikhin · Vladislav V. Kharton

Received: 7 September 2010 / Accepted: 21 September 2010 / Published online: 5 October 2010
© Springer-Verlag 2010

Abstract Increasing Sr^{2+} and Ti^{4+} concentrations in perovskite-type $(La_{0.75-x}Sr_{0.25+x})_{0.95}Mn_{0.5}Cr_{0.5-x}Ti_xO_{3-\delta}$ $(x = 0 - 0.5)$ results in slightly higher thermal and chemical expansion, whereas the total conductivity activation energy tends to decrease. The average thermal expansion coefficients determined by controlled-atmosphere dilatometry vary in the range $(10.8–14.5)\times10^{-6}$ K^{-1} at 373–1,373 K, being almost independent of the oxygen partial pressure. Variations of the conductivity and Seebeck coefficient, studied in the oxygen pressure range 10^{-18}–0.5 atm, suggest that the electronic transport under oxidizing and moderately reducing conditions is dominated by p-type charge carriers and occurs via a small-polaron mechanism. Contrary to the hole concentration changes, the hole mobility decreases with increasing x. The oxygen permeation fluxes through dense ceramic membranes are quite similar for all compositions due to very low level of oxygen nonstoichiometry and are strongly affected by the grain-boundary diffusion and surface exchange kinetics. The porous electrodes applied onto lanthanum gallate-based solid electrolyte exhibit a considerably better electrochemical performance compared to the apatite-type $La_{10}Si_5AlO_{26.5}$ electrolyte at atmospheric oxygen pressure, while Sr^{2+} and Ti^{4+} additions have no essential influence on the polarization resistance. In H_2-containing gases where the electronic transport in $(La_{0.75-x}Sr_{0.25+x})_{0.95}Mn_{0.5}Cr_{0.5-x}$ $Ti_xO_{3-\delta}$ perovskites becomes low, co-doping deteriorates the anode performance, which can be however improved by infiltrating Ni and $CeO_{2-\delta}$v into the porous oxide electrode matrix.

Keywords SOFC electrode · Anodic polarization · Electronic transport · Mixed conductivity · Oxygen permeability · Dilatometry · Electrochemical activity · Thermomechanical compatibility

V. A. Kolotygin · E. V. Tsipis · A. L. Shaula · E. N. Naumovich · J. R. Frade · V. V. Kharton (✉)
Department of Ceramics and Glass Engineering, CICECO,
University of Aveiro,
3810-193 Aveiro, Portugal
e-mail: kharton@ua.pt

E. V. Tsipis
Chemistry Department,
Instituto Tecnológico e Nuclear, CFMC-UL,
EN 10,
2686-953 Sacavém, Portugal

A. L. Shaula
Department of Mechanical Engineering, SEG-CEMUC,
University of Coimbra,
3030-788 Coimbra, Portugal

S. I. Bredikhin
Institute of Solid State Physics RAS,
Institutskaya 2,
142432 Chernogolovka, Moscow, Russia

Introduction

One important challenge in the developments of solid oxide fuel cells (SOFCs), high-temperature electrolyzers of steam and carbon dioxide, and SOFC-based electrocatalytic reactors relates to the search for electrochemically active electrode materials stable in both reducing and oxidizing atmospheres [1–4]. In addition to the electrochemical properties, critical requirements to the fuel electrode materials include a high electronic conductivity, thermodynamic stability under fabrication and operation conditions of the electrochemical cells, catalytic activity towards oxidation of hydrocarbons and other C-containing species enabling to suppress carbon deposition, thermomechanical

and chemical compatibility with solid electrolyte ceramics, and low costs. The conventional Ni-based cermet anodes exhibit serious disadvantages, primarily fast coking in hydrocarbon-fueled SOFCs and large volume changes on redox cycling, leading to degradation. These problems may be solved by replacing nickel with other metals having a low catalytic activity towards coking and/or by using ceramic-based electrodes with zero or small amounts of metallic components [3–14]. The well-known parent oxide systems, extensively studied for the development of reliable SOFC anodes, are perovskite-related titanates and chromites stable in relatively wide ranges of the oxygen partial pressures, $p(O_2)$ [3, 6–8]. The performance of titanate- and chromite-based electrodes is often, however, very poor. In particular, strontium–lanthanum titanates exhibit a substantially high electronic conduction at low $p(O_2)$ but tend to degrade due to oxidation; perovskite-type $(La, Sr)CrO_{3-\delta}$ and their derivatives suffer from low electrochemical activity, volatilization of Cr-containing species, poor conductivity in reducing atmospheres, and, in some cases, weak adherence to the solid electrolyte ceramics.

These disadvantages are less pronounced in the case of $(La_{0.75}Sr_{0.25})_{1-y}Cr_{0.5}Mn_{0.5}O_{3-\delta} (y = 0 - 0.05)$ perovskites [9–16]. Nevertheless, the electrochemical performance of $(La_{0.75}Sr_{0.25})_{1-y}Cr_{0.5}Mn_{0.5}O_{3-\delta}$ electrodes in both reducing and oxidizing atmospheres is essentially limited by the electronic conduction [15]. As a result, such anodes and cathodes without any additional components display relatively high overpotentials; the incorporation of metals (e.g., Ni, Cu, or Ag) and/or electrocatalytically active additives (e.g., ceria in reducing atmospheres or praseodymia in air) decreases electrode resistance [12–15]. For example, ceria infiltration into porous $(La_{0.75}Sr_{0.25})_{0.95}Cr_{0.5}Mn_{0.5}O_{3-\delta}$ anode applied on a $(La_{0.9}Sr_{0.1})_{0.98}Ga_{0.8}Mg_{0.2}O_{3-\delta}$ (LSGM) solid electrolyte with $Ce_{0.8}Gd_{0.2}O_{2-\delta}$ (CGO) interfacial layer lowers the overpotential from ~178 down to 97 mV at 1073 K and 70 mA/cm^2 in humidified 10% H_2–90% N_2 mixture [15]. Notice also that positive influence of CGO interlayers is widely known in the literature (e.g., [3, 9] and references cited); in particular, introducing a ceria-based buffer layer between lanthanum gallate-based electrolyte and $La_{0.75}Sr_{0.25}Cr_{0.5}Mn_{0.5}O_{3-\delta}$ electrodes enables to prevent diffusion of Cr and Mn cations into the electrolyte surface layers [14]. This diffusion and a high volatility of Cr-containing species make it necessary to avoid the presence of chromium or, at least, to decrease its content in the electrode materials [14]. One possible strategy may relate to the replacement of chromium in $(La_{0.75}Sr_{0.25})_{1-y}Cr_{0.5}Mn_{0.5}O_{3-\delta}$ with other transition metal cations having a relatively stable oxidation state in both reducing and oxidizing conditions, in combination with aliovalent doping for change compensation enabling to preserve the lattice conservation condition.

The present work is centered on the appraisal of perovskite-type $(La_{0.75-x}Sr_{0.25+x})_{0.95}Mn_{0.5}Cr_{0.5-x}Ti_xO_{3-\delta}$ $(x = 0 - 0.5)$ system. Primary emphasis is given to the properties relevant for the electrode applications, including phase stability in various atmospheres, mixed conductivity, thermal and chemical expansion, and electrochemical behavior of porous layers. The solid electrolytes selected for this case study, perovskite-type LSGM and apatite-type $La_{10}Si_5AlO_{26.5}$, have been characterized in previous works [17, 18]. The data on parent $(La_{0.75}Sr_{0.25})_{0.95}Cr_{0.5}Mn_{0.5}O_{3-\delta}$ studied earlier [15] are used for the sake of comparison.

Experimental

Submicron powders of $(La_{0.75-x}Sr_{0.25+x})_{0.95}Mn_{0.5}Cr_{0.5-x}Ti_xO_{3-\delta}$ were prepared by mixing of the stoichiometric amounts of high-purity $La(NO_3)_3{\cdot}6H_2O$, $Sr(NO_3)_2$, $Mn(CH_3COO)_2{\cdot}4H_2O$, $Cr(NO_3)_3{\cdot}9H_2O$, TiO_2, and glycine, with subsequent drying and self-combustion. Then the

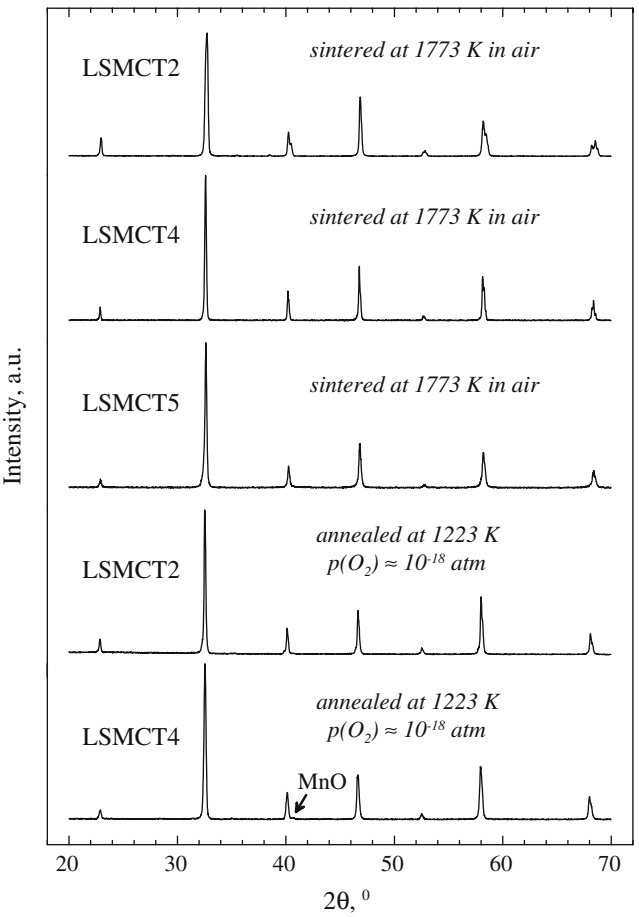

Fig. 1 XRD patterns of $(La_{0.75-x}Sr_{0.25+x})_{0.95}Mn_{0.5}Cr_{0.5-x}Ti_xO_{3-\delta}$ after sintering in air at 1773 K and after reduction in flowing H_2–H_2O–N_2 gas mixture with $p(O_2) \approx 10^{-18}$ atm at 1223 K during 25 h

Table 1 Abbreviations, unit cell parameters, and density of $(La_{0.75-x}Sr_{0.25+x})_{0.95}Mn_{0.5}Cr_{0.5-x}Ti_xO_{3-\delta}$ ceramics

Composition	Abbreviation	*a*, Å	*c*, Å	*V*, Å ^{3}	ρ_{theor}, g/cm^3	ρ_{exp}, g/cm^3	Relative density,%
$(La_{0.75}Sr_{0.25})_{0.95}Mn_{0.5}Cr_{0.5}O_{3-\delta}$	LSMCT0	5.4953 (2)	13.3098 (6)	348.08 (4)	6.03	5.99	99.3
$(La_{0.55}Sr_{0.45})_{0.95}Mn_{0.5}Cr_{0.3}Ti_{0.2}O_{3-\delta}$	LSMCT2	5.4955 (3)	13.3738 (8)	349.78 (6)	6.00	5.74	95.7
$(La_{0.45}Sr_{0.55})_{0.95}Mn_{0.5}Cr_{0.2}Ti_{0.3}O_{3-\delta}$	LSMCT3	5.4992 (1)	13.4138 (7)	351.30 (4)	5.83	5.57	95.6
$(La_{0.35}Sr_{0.65})_{0.95}Mn_{0.5}Cr_{0.1}Ti_{0.4}O_{3-\delta}$	LSMCT4	5.4963 (1)	13.4266 (3)	351.27 (2)	5.68	5.47	96.4
$(La_{0.25}Sr_{0.75})_{0.95}Mn_{0.5}Ti_{0.5}O_{3-\delta}$	LSMCT5	5.4960 (8)	13.4551 (1)	351.97 (1)	5.52	5.18	94.0

a, *c*, and *V* are the unit cell parameters and volume, respectively

ρ_{theor} theoretical densities, ρ_{exp} experimental densities

foam-like products were calcined in air at 1073 K for 2 h, ball-milled, and pressed into disks. Gas-tight ceramics with 94–97% density were sintered in air at 1773 K for 10–15 h and slowly cooled (2–3 K/min) in order to provide equilibration with atmospheric oxygen at low temperatures. To assess the influence of grain size on the oxygen permeability, a series of ceramic samples with x=0.4 were also sintered at the same temperature for 50 h. The processing conditions of LSGM and $La_{10}Si_5AlO_{26.5}$ electrolyte ceramics were reported in Refs. [17, 18]. The porous

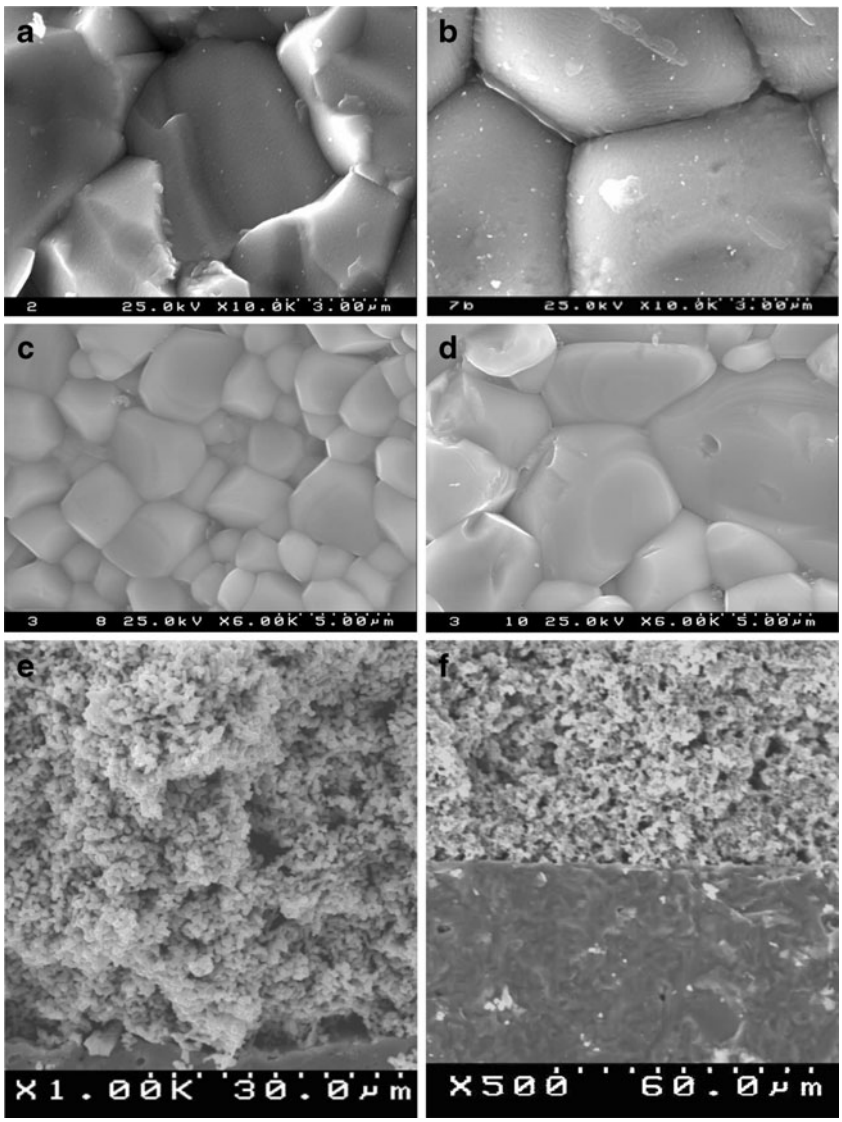

Fig. 2 SEM micrographs of fractured LSMCT3 (**a**), LSMCT5 (**b**), and LSMCT4 (**c** and **d**) ceramics, LSMCT0 electrode applied onto LSGM and then surface-modified with $CeO_{2-\delta}$ and Ni (**e**), and PrO_x-modified LSMCT5 electrode in contact with $La_{10}Si_5AlO_{26.5}$ electrolyte (**f**). **c** and **d** compare the microstructures of LSMCT4 ceramics sintered during 15 and 50 h, respectively. The micrographs of the half-cells (**e** and **f**) were collected after the electrochemical measurements in 10% H_2–N_2–H_2O and air, correspondingly

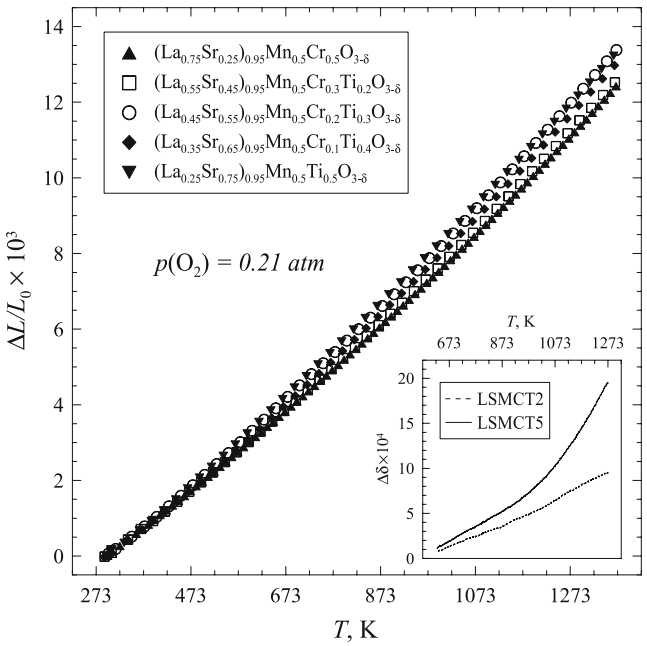

Fig. 3 Dilatometric curves of $(La_{0.75-x}Sr_{0.25+x})_{0.95}Mn_{0.5}Cr_{0.5-x}Ti_xO_{3-\delta}$ ceramics in air. *Inset* compares the oxygen nonstoichiometry variations in LSMCT2 and LSMCT5, collected by TGA on heating in dried air. L_0 is the sample length at room temperature

electrode layers (sheet density of 7–10 mg/cm^2) with 2 wt. % Bi_2CuO_4 sintering aid were deposited onto the electrolyte substrates and annealed in air at 1473 K for 2 h. Prior to the deposition of all anodes, an intermediate CGO layer (3–5 mg/cm^2) was applied onto the solid electrolyte surface and fired at 1473 K for 2 h. The electrode fabrication procedures and cell geometry were similar to those reported elsewhere [15]. Formation of single perovskite phases in dense $(La_{0.75-x}Sr_{0.25+x})_{0.95}Mn_{0.5}Cr_{0.5-x}Ti_xO_{3-\delta}$ ceramics and porous electrodes was confirmed by X-ray diffraction (XRD) analysis. General characterization included also scanning electron microscopy coupled with energy-dispersive spectroscopy (SEM/EDS), controlled-atmosphere dilatometry, thermogravimetric analysis (TGA), measurements of total electrical conductivity (four-probe DC) and Seebeck coefficient as functions of the oxygen partial pressure and temperature, and determination of the steady-state oxygen permeability (OP). Description of the experimental techniques and equipment used is found elsewhere ([5, 15, 17–20] and references cited). For all OP data presented in this work, the oxygen partial pressure at the membrane feed side (p_2) corresponds to 0.21 atm. The dilatometric measurements were performed on heating with a constant rate of 3 K/min and in the regime of temperature cycling in the range 923–1223 K with 50 K steps and dwells at each temperature during 2–7 h.

The studies of steady-state electrode polarization were carried out by the three-electrode technique in the cells with porous Pt counter and reference electrodes (CE and RE) and Pt gauze current collectors, as described in [5, 15, 19]. The experiments were carried out in the galvanostatic mode using PGSTAT20 and PGSTAT302 Autolab instruments at 873–1,073 K in flowing air or wet 10% H_2–N_2. After the measurements, selected electrode layers were surface-modified [5, 15, 19] with nickel and cerium oxide (for anodes) or praseodymium oxide (for cathodes) via impregnation with saturated ethanol solutions of the metal nitrates; following an additional calcination step at 1100–1150 K for 2 h, the overpotential-current dependencies were re-measured. The tested electrodes were examined by XRD and SEM/EDS in order to reveal possible structural and microstructural changes.

Results and discussion

Structure, microstructure, and dimensional stability

XRD analysis showed the continuous solid solution formation in the entire $(La_{0.75-x}Sr_{0.25+x})_{0.95}Mn_{0.5}Cr_{0.5-x}$

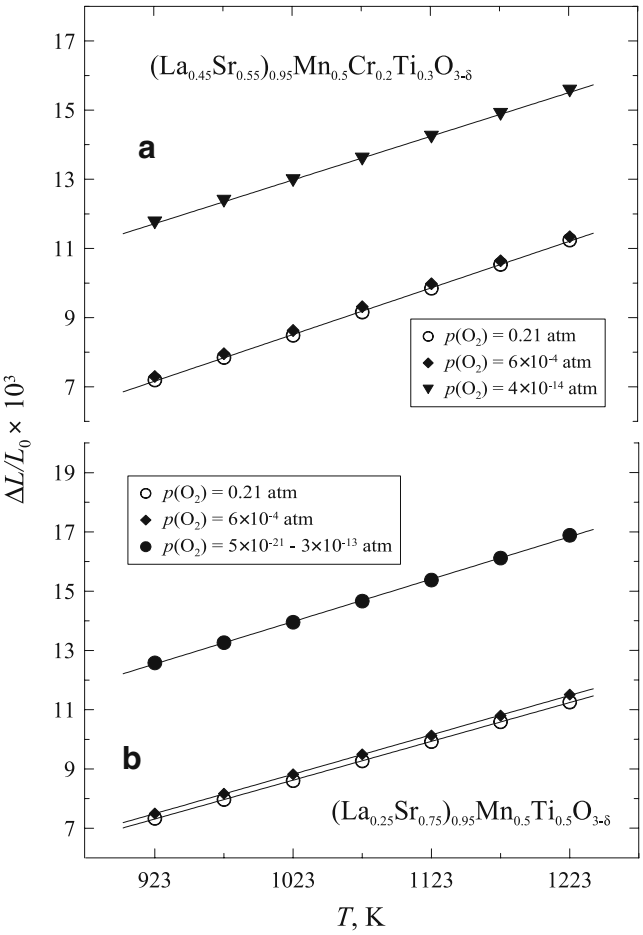

Fig. 4 Temperature dependencies of the relative length changes of LSMCT3 (**a**) and LSMCT5 (**b**) ceramics in air, Ar–O_2 and CO–CO_2 atm

Table 2 Average linear thermal expansion coefficients of $(La_{0.75-x}Sr_{0.25+x})_{0.95}Mn_{0.5}Cr_{0.5-x}Ti_xO_{3-\delta}$ ceramics

Abbreviation	$p(O_2)$, atm	T, K	TEC×10^6, K^{-1}
LSMCT0	0.21	373–923	10.8±0.1
	0.21	923–1223	12.7±0.2
	6×10^{-4}	923–1223	12.5±0.3
	5×10^{-21}–3×10^{-13}	923–1223	11.7±0.2
	0.21	1223–1523	14.1±0.1
LSMCT2	0.21	303–923	10.8±0.1
	0.21	923–1223	12.8±0.1
	0.21	1223–1373	13.6±0.1
LSMCT3	0.21	303–923	11.6±0.1
	0.21	923–1223	13.5±0.1
	6×10^{-4}	923–1223	13.5±0.1
	4×10^{-14}	923–1223	12.7±0.3
	0.21	1,223–1373	14.5±0.1
LSMCT4	0.21	293–923	11.2±0.1
	0.21	923–1223	13.1±0.1
	0.21	1,223–1373	14.1±0.1
LSMCT5	0.21	303–923	11.8±0.1
	0.21	923–1223	13.1±0.1
	6×10^{-4}	923–1223	13.3±0.2
	5×10^{-21}–3×10^{-13}	923–1223	14.3±0.1
	0.21	1,223–1373	14.0±0.1

$Ti_xO_{3-\delta}(x = 0 - 0.5)$ system under oxidizing conditions. As for parent $(La_{0.75}Sr_{0.25})_{0.95}Cr_{0.5}Mn_{0.5}O_{3-\delta}$, the perovskite-type crystal structure of Ti-containing compositions was identified as rhombohedrally distorted (space group $R\bar{3}c$). Selected XRD patterns are presented in Fig. 1. Table 1 lists the unit cell parameters in hexagonal settings and abbreviations used below. The unit cell volume tends to slightly increase with increasing x, as expected from the cation radius variations. In agreement with literature data [9, 10, 21, 22], reducing $p(O_2)$ down to 10^{-18} atm does not lead to perovskite decomposition (Fig. 1), except for the segregation of minor amounts of MnO. Note that MnO segregation was also reported on reduction of $La_{0.75}Sr_{0.25}Cr_{0.5}Mn_{0.5}O_{3-\delta}$ [22].

Typical microstructures of $(La_{0.75-x}Sr_{0.25+x})_{0.95}Mn_{0.5}Cr_{0.5-x}Ti_xO_{3-\delta}$ dense ceramics and porous electrodes are illustrated in Fig. 2. SEM inspection of the ceramic materials showed traces of glassy phases at the grain boundaries, suggesting a liquid phase-assisted sintering process. At the same time, no compositional inhomogeneities were revealed by EDS, within the limit of experimental uncertainty. As expected, increasing sintering time leads to a larger grain size (Fig. 2c, d).

The results of dilatometric measurements are summarized in Figs. 3 and 4 and Tables 2, 3, 4. The average linear thermal expansion coefficients (TECs) vary in the range $(10.8–14.5)\times10^{-6}$ K^{-1}, similar to other chromite- and manganite-based materials [1, 3, 20], and seem almost independent of the oxygen partial pressure. However, careful examination of the thermal expansion data shows that the TECs tend to a modest increase with strontium and titanium additions. This increase correlates with increasing oxygen nonstoichiometry variations on doping (inset in Fig. 3) and might be, therefore, associated with decreasing average oxidation state of manganese cations. At the same time, the TGA data suggest that even for $(La_{0.25}Sr_{0.75})_{0.95}Mn_{0.5}Ti_{0.5}O_{3-\delta}$, the oxygen losses on heating in air are very minor; hence, chemical contribution to the thermal expansion should be almost negligible. Therefore, the increase in TEC values with temperature and x (Fig. 3 and Table 2) results primarily from shifting redox equilibria in the perovskite lattice. Namely, co-doping with Sr^{2+} and Ti^{4+} seems to promote high-temperature disproportionation of manganese, $2Mn^{3+} \Leftrightarrow Mn^{4+} + Mn^{2+}$; increasing concentration of the p-type electronic change carriers facilitates oxygen losses on heating. Such a hypothesis is in agreement with the variations of electronic conductivity and Seebeck coefficient, discussed below. Notice also that the changes in TECs, oxygen nonstoichiometry, and chemical expansivity induced by co-doping exhibit a correlation with the unit cell volume (Table 1).

As for the parent material, $(La_{0.75}Sr_{0.25})_{0.95}Cr_{0.5}Mn_{0.5}O_{3-\delta}$ [15], the chemically induced expansion of Ti-substituted compositions on decreasing $p(O_2)$ down to 6×10^{-4} atm is lower than 0.03% (Fig. 4 and Table 3). In

Table 3 Chemically induced strain of $(La_{0.75-x}Sr_{0.25+x})_{0.95}Mn_{0.5}Cr_{0.5-x}Ti_xO_{3-\delta}$ ceramics, measured on reducing $p(O_2)$ from 0.21 atm down to 6×10^{-4} atm

Abbreviation	$(L\text{-}L^{air})/L^{air}\times10^3$						
	923 K	973 K	1023 K	1073 K	1123 K	1173 K	1223 K
LSMCT0	0.20	0.23	0.19	0.15	0.14	0.15	0.17
LSMCT3	0.10	0.11	0.14	0.16	0.13	0.11	0.09
LSMCT5	0.17	0.20	0.21	0.22	0.20	0.21	0.25

The expansion is given with respect to the length in air at a given temperature (L^{air})

Table 4 Chemically induced strain of $(La_{0.75-x}Sr_{0.25+x})_{0.95}Mn_{0.5}Cr_{0.5-x}Ti_xO_{3-\delta}$ ceramics in reducing atmospheres

T, K	LSMCT0		LSMCT3		LSMCT5	
	$p(O_2)$, atm	$(L\text{-}L^{air})/L^{air}\times10^3$	$p(O_2)$, atm	$(L\text{-}L^{air})/L^{air}\times10^3$	$p(O_2)$, atm	$(L\text{-}L^{air})/L^{air}\times10^3$
923	5×10^{-21}	2.25	4×10^{-14}	4.51	5×10^{-21}	5.21
973	2×10^{-19}	2.30	4×10^{-14}	4.49	2×10^{-19}	5.25
1023	6×10^{-18}	2.21	4×10^{-14}	4.44	6×10^{-18}	5.30
1073	1×10^{-16}	2.12	4×10^{-14}	4.39	1×10^{-16}	5.34
1123	2×10^{-15}	2.08	4×10^{-14}	4.33	2×10^{-15}	5.40
1173	3×10^{-14}	2.04	4×10^{-14}	4.30	3×10^{-14}	5.47
1223	3×10^{-13}	2.01	4×10^{-14}	4.26	3×10^{-13}	5.56

reducing atmospheres, the lattice expansion increases and achieves almost 0.6% with respect to the atmospheric oxygen pressure (Table 4), a result of increasing oxygen-vacancy concentration and the corresponding changes of B-site cation oxidation state. The latter processes, responsible for increasing B-site cation radii, are indicated by the conductivity drop at low $p(O_2)$ [15, 21, 22]. Again, the chemical expansion of $(La_{0.75-x}Sr_{0.25+x})_{0.95}Mn_{0.5}Cr_{0.5-x}Ti_xO_{3-\delta}$ increases with increasing x since Sr and Ti co-doping promotes oxygen losses (Fig. 5). The overall level of thermal (ε_T) and chemical (ε_C) induced strains observed in the wide range of temperature and oxygen partial pressure is moderate, making it possible to use the title materials in contact with solid oxide electrolytes, such as stabilized zirconia, CGO, LSGM, or $La_{10}Si_5AlO_{26.5}$ [17, 18, 23]. Nonetheless, one should still be cautious concerning the strains at elevated temperatures necessary to fabricate electrochemical cells. For example, cooling of $(La_{0.25}Sr_{0.75})_{0.95}Mn_{0.5}Ti_{0.5}O_{3-\delta}$ from 1373 to 973 K in air leads to the contraction within $\varepsilon_T\approx-0.54\%$, which is only differs from that for typical solid electrolytes. If assuming that a relatively thin selectrolyte layer with a TEC of 11.1×10^{-6} K^{-1} is fired onto a thick LSMCT5 substrate, reaching an unstrained condition at 1373 K in air, the expected strain difference after cooling down to 973 K is in the order of $\Delta\varepsilon\approx0.10\%$. The compressive stresses imposed on the thin solid-electrolyte layer can then be estimated as $\sigma_C \approx \Delta\varepsilon E/(1-\nu) \approx -179$ MPa, using typical values of the elastic constants E=125 GPa and $\nu\approx0.3$ known for LSGM at 973 K [24]. These low and compressive stresses should be acceptable for applications of the electrochemical cells. However, the thermal and

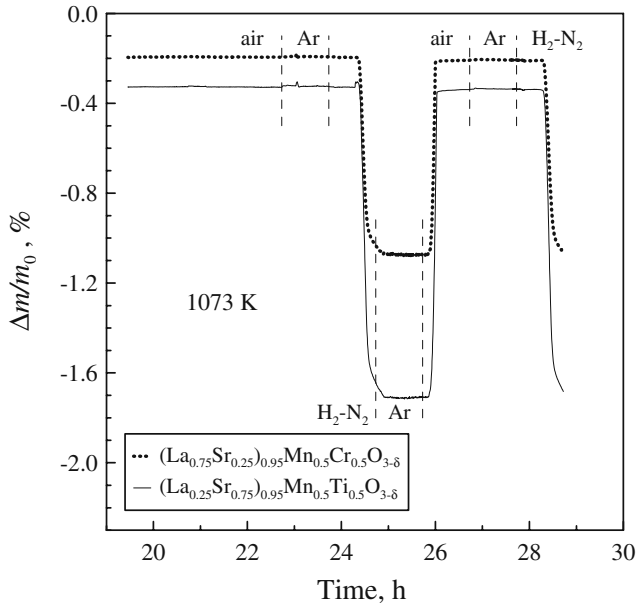

Fig. 5 Comparison of the relative weight changes of $(La_{0.75}Sr_{0.25})_{0.95}Mn_{0.5}Cr_{0.5}O_{3-\delta}$ and $(La_{0.25}Sr_{0.75})_{0.95}Mn_{0.5}Ti_{0.5}O_{3-\delta}$ on cycling of the oxygen chemical potential in the gaseous phase, measured by TGA. m_0 is the initial weight of the samples equilibrated with atmospheric oxygen at low temperatures

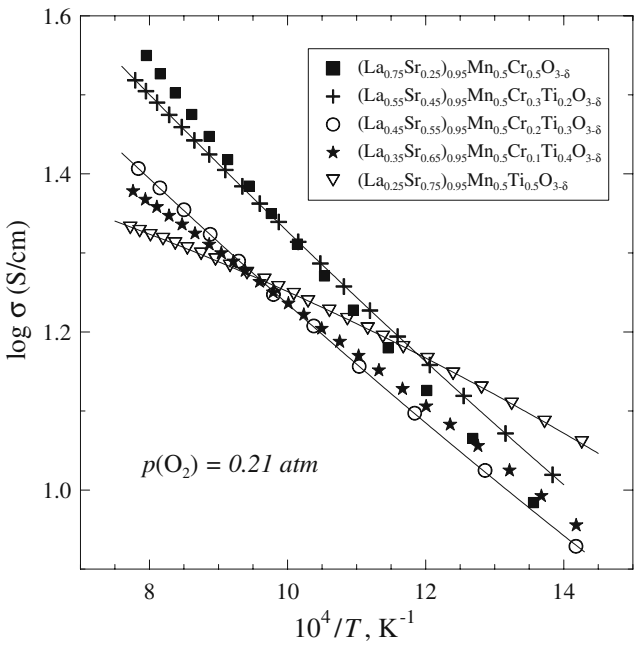

Fig. 6 Temperature dependencies of the total conductivity of $(La_{0.75-x}Sr_{0.25+x})_{0.95}Mn_{0.5}Cr_{0.5-x}Ti_xO_{3-\delta}$ ceramics in air

Table 5 Activation energies for the total conductivity of $(La_{0.75-x}Sr_{0.25+x})_{0.95}Mn_{0.5}Cr_{0.5-x}Ti_xO_{3-\delta}$ at atmospheric $p(O_2)$

Abbreviation	T, K	E_a, kJ/mol
LSMCT0	553–873	22.6±0.5
	943–1263	29.8±0.6
LSMCT2	553–873	20.3±0.4
	943–1263	25.6±0.3
LSMCT3	643–903	20.0±0.8
	943–1273	24.4±0.8
LSMCT4	553–873	20.2±0.2
	943–1263	21.4±0.1
LSMCT5	553–873	15.6±0.1
	943–1263	16.1±0.1

chemical strain components of $(La_{0.25}Sr_{0.75})_{0.95}Mn_{0.5}Ti_{0.5}O_{3-\delta}$ almost compensate each other under reducing conditions, for instance, $(\varepsilon_T + \varepsilon_C) \approx -0.02\%$ at 973 K and $p(O_2) = 2 \times 10^{-19}$atm. Under these conditions, the strain difference between the layers becomes $\Delta\varepsilon \approx -0.44\%$, imposing excessive tensile stresses on the thin electrolyte layer (for the above-quoted elastic constants, $\sigma_C \approx 786$ MPa). On the other hand, actual stresses may be significantly lower when one of the contacting layers is very porous, as for the deposition of a thin porous electrode onto a thicker solid-electrolyte support. In the latter case, the stresses under reducing conditions revert from tensile to compressive, thus providing better thermomechanical stability.

Electrical conductivity and Seebeck coefficient

Figure 6 displays the temperature dependencies of total conductivity (σ) of $(La_{0.75-x}Sr_{0.25+x})_{0.95}Mn_{0.5}Cr_{0.5-x}Ti_xO_{3-\delta}$ at atmospheric $p(O_2)$. The conductivity is predominantly electronic; the oxygen permeation data presented below show that the oxygen-ionic contribution is lower than 10^{-3}%. In air, the conductivity has a thermally activated character with the activation energies (E_a) of 16–30 kJ/mol at 943–1263 K (Table 5), decreasing on Sr and Ti co-doping. Such behavior might indicate a tendency to the transition from the small-polaron hopping mechanism typical for $LaCrO_3$- and $LaMnO_3$-based compounds [15, 22, 25], to the broadband conduction mechanism typical for doped $SrTiO_{3-\delta}$ and $SrMnO_{3-\delta}$ (e.g., see [20, 25] and references cited). This transition should correlate with decreasing activation energies for the mobility of electronic charge carriers; temperature dependencies of the charge-carrier concentration should be governed by two factors having opposite effects, namely thermal excitation and increasing oxygen deficiency when temperature increases.

The oxygen partial pressure dependencies of the electrical properties (Figs. 7 and 8) exhibit a series of specific features typical for $LaMnO_3$- and $LaCrO_3$-based solid

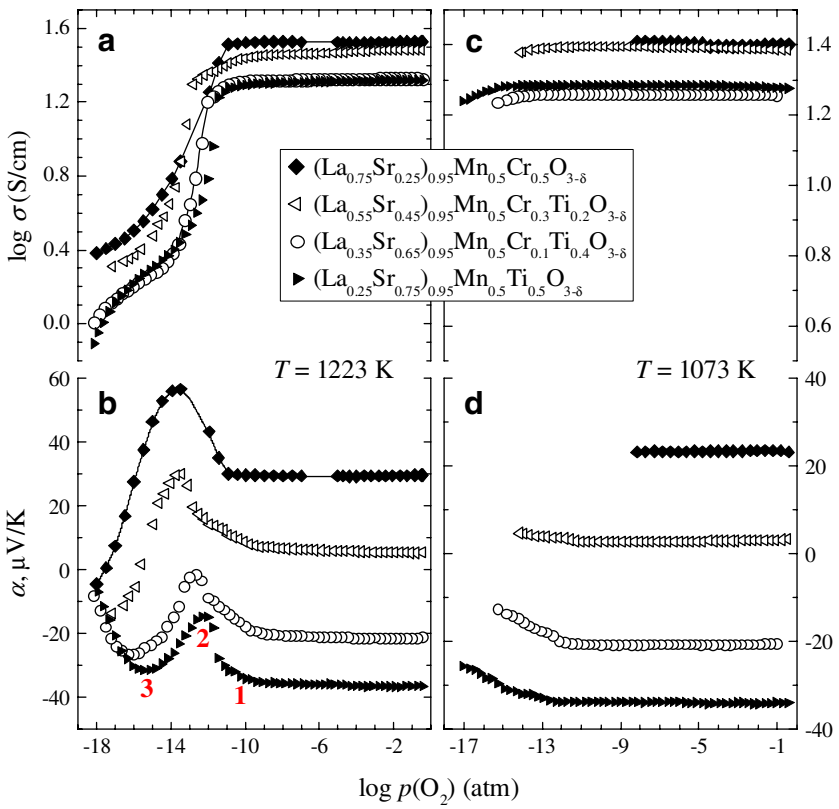

Fig. 7 Oxygen partial pressure dependencies of the total conductivity (**a**, **c**) and Seebeck coefficient (**b**, **d**) of $(La_{0.75-x}Sr_{0.25+x})_{0.95}Mn_{0.5}Cr_{0.5-x}Ti_xO_{3-\delta}$ at 1223 K (**a**, **b**) and 1073 K (**c**, **d**). The numbers **1**, **2**, and **3** (**b**) show characteristic conditions where changes in the redox behavior are observed (see text)

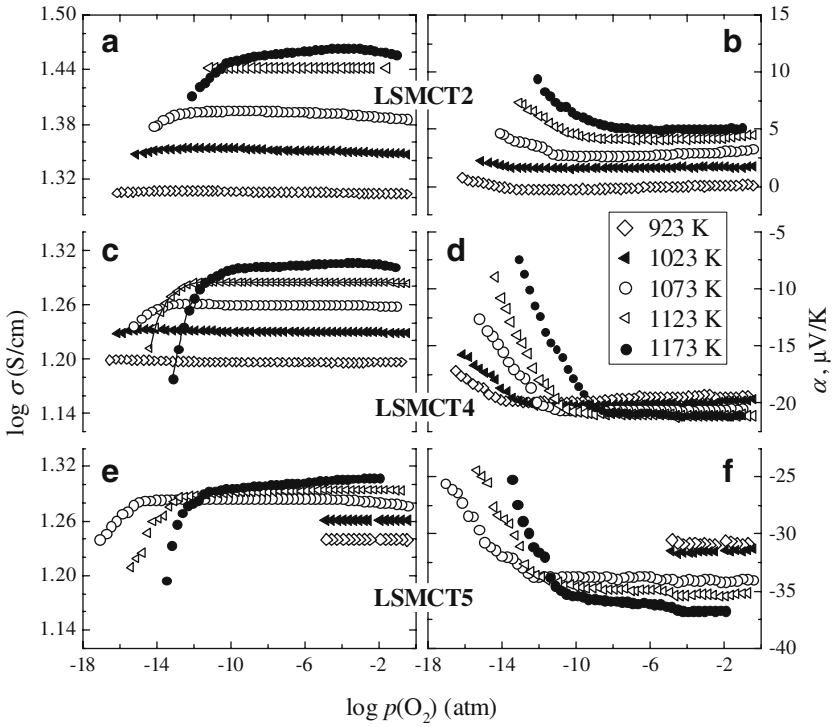

Fig. 8 Oxygen partial pressure dependencies of the total conductivity and Seebeck coefficient of LSMCT2 (**a**, **b**), LSMCT4 (**c**, **d**), and LSMCT5 (**e**, **f**)

solutions [15, 25, 26]. First of all, both the Seebeck coefficient (α) and conductivity are essentially $p(O_2)$-independent in oxidizing and moderately reducing environments, indicating that the oxygen stoichiometry changes are minor. Increasing x lowers the thermopower down to negative values at $x>0.2$. This trend is not surprising taking into account that strontium titanate exhibits n-type electronic transport (e.g., [6, 7] and references therein). However, reducing oxygen pressure below a certain level, marked as "**1**" in Fig. 7b, gives rise to increasing oxygen deficiency, which results in increasing Seebeck coefficient and decreasing conductivity. This type of behavior observed for all compositions provides an argument in favor of dominant p-type electronic transport, despite the negative α values for Sr- and Ti-rich materials. Comparison of the corresponding oxygen pressures (Fig. 9) with the low-$p(O_2)$ stability limits of Cr-, Mn-, and Ti-containing oxide phases [27–30] suggests that these phenomena are mainly associated with reduction of manganese cations rather than with phase decomposition, in agreement with XRD. Notice also that the fact, that the corresponding $p(O_2)$ values are essentially independent of x in $(La_{0.75-x}Sr_{0.25+x})_{0.95}Mn_{0.5}Cr_{0.5-x}Ti_xO_{3-\delta}$, indicates that the electronic transport processes and oxygen deficiency variations are determined by the B sites occupied by manganese, whereas Cr and Ti cations form a redox-stable matrix.

Furthermore, in oxidizing and mildly reducing atmospheres the Seebeck coefficient increases with temperature for the compositions with x=0–0.2 but exhibits a slight opposite tendency when x increases up to 0.4–0.5 (Figs. 7 and 8). Possible origin of the thermopower variations in $(La_{0.75}Sr_{0.25})_{0.95}Cr_{0.5}Mn_{0.5}O_{3-\delta}$, associated with shifting the redox equilibrium between Cr and Mn cations and site-exclusion effects, was discussed in previous work [15]. In the case of $(La_{0.75-x}Sr_{0.25+x})_{0.95}Mn_{0.5}Cr_{0.5-x}Ti_xO_{3-\delta}$ $(x = 0.4 - 0.5)$, all titanium cations under oxidizing conditions are expected to have constant oxidation state, 4+; the site-exclusion phenomena near Ti^{4+}, if any, should remain essentially unchanged when temperature increases. Since the relative variations of oxygen nonstoichiometry with temperature (inset in Fig. 3) are much smaller than those of thermopower, the decrease in Seebeck coefficient originates from thermal excitation of p-type electronic charge carriers in accordance with the Heikes formula [25, 30, 31]:

$$\alpha = \frac{k}{e} \cdot \ln \frac{N-p}{p} \tag{1}$$

where p is the mobile hole concentration, N is the number of states, and any spin-degeneracy phenomena and transported heat of holes are neglected. The (p/N) values calculated by Eq. 1 were also used to evaluate the variations of hole mobility (μ_p) from the conductivity data:

$$\sigma = ep\mu_p \cdot N_{fu}/V_{uc} \tag{2}$$

where N_{fu} is the number of formula units per unit cell, V_{uc} is the unit-cell volume, and p is related to formula unit.

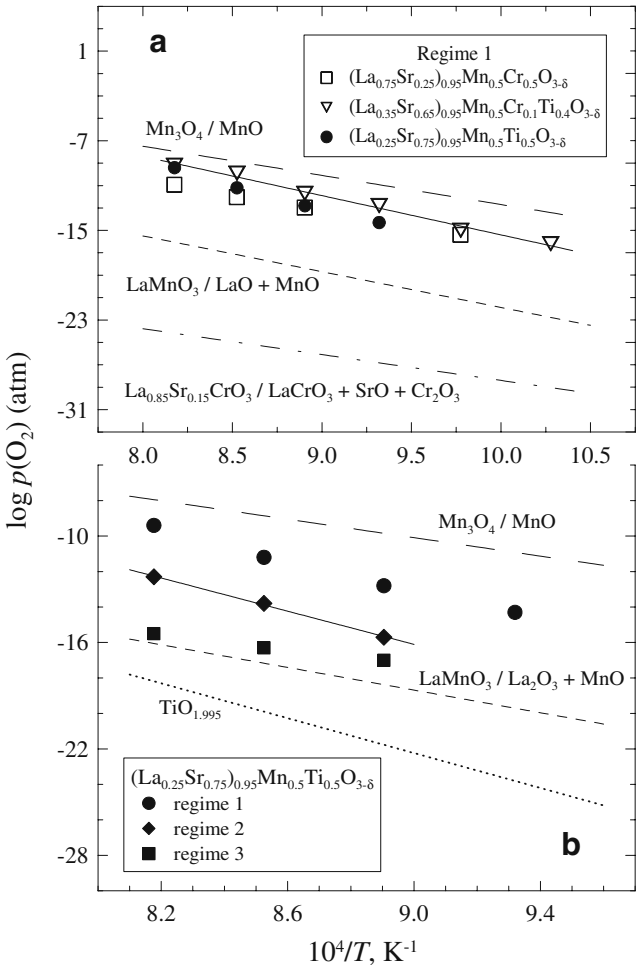

Fig. 9 Oxygen partial pressures corresponding to the changes in redox behavior, marked as **1**, **2**, and **3** in Fig. 6b. Literature data on the phase stability limits of Cr- and Mn-containing oxide phases [27–29] and iso-stoichiometric line for $TiO_{1.995}$ [30] are shown for comparison

The estimates of (p/N) and ($\mu_p \times N$) are plotted in Figs. 10 and 11.

For all studied materials, the hole mobility is temperature-activated (Fig. 11a). This makes it possible to conclude that small-polaron mechanism is dominant, irrespective of the progressive decrease in the mobility activation energy indicating an increasing role of the broadband mechanism on doping. In the case of $(La_{0.75}Sr_{0.25})_{0.95}Cr_{0.5}Mn_{0.5}O_{3-\delta}$, the ($p/N$) ratio decreases with increasing temperature as the equilibrium between the B-site cations ($Cr^{4+} + Mn^{3+}Cr^{3+} + Mn^{4+}$) shifts towards Mn^{4+} formation and the site-blocking effects near Cr^{4+} disappear [15]; $(La_{0.25}Sr_{0.75})_{0.95}Mn_{0.5}Ti_{0.5}O_{3-\delta}$ exhibit a modest but clearly visible opposite trend (Figs. 10e and 11b). If considering the stable oxidation state of Ti^{4+} under oxidizing conditions, rising (p/N) with temperature provides an evidence for progressive Mn^{3+} disproportionation, leading to Mn^{4+} and Mn^{2+} formation on heating. The increasing Mn^{4+} concentration is responsible for higher oxygen losses and for the larger chemical and thermal expansion observed for Ti- and Sr-rich compositions (Fig. 3 and Table 4). Also, the variations in Seebeck coefficient, which becomes negative on co-doping, originate primarily from increasing Mn^{4+} concentration. Under oxidizing conditions when the oxygen nonstoichiometry is very low, the occupancy of manganese sites available for hole hopping (p/N) in $(La_{0.25}Sr_{0.75})_{0.95}Mn_{0.5}Ti_{0.5}O_{3-\delta}$ is higher than 50%. The latter factor contributes also to the relatively low hole mobility which decreases on Ti and Sr co-doping, mainly due to blocking of electronic transfer by the redox stable Ti^{4+} cations (Figs. 10 and 11).

At oxygen partial pressures below approximately 10^{-13} atm, the slope of the σ vs. $p(O_2)$ curves decreases (Fig. 7a); the Seebeck coefficient of Ti-rich compositions exhibits a maximum and a minimum marked in Fig. 7b as "**2**" and "**3**," respectively. Most likely, these regimes are associated with rising contributions of the $Mn^{3+/2+}$ and $Ti^{4+/3+}$ redox couples. However, due to phase transitions known for $(La, Sr)(Mn, Cr)O_{3-\delta}$ perovskites on reduction [9, 10, 21, 22] and to the segregation of MnO traces (Fig. 2), quantitative analysis of the electrical properties in this $p(O_2)$ range is problematic. Irrespective of the microscopic mechanisms, co-doping with Sr and Ti leads to lower conductivity under reducing conditions. This effect is expected to further increase the role of electronic transport as the electrode performance-limiting factor, characteristic of parent $(La_{0.75}Sr_{0.25})_{0.95}Cr_{0.5}Mn_{0.5}O_{3-\delta}$ [15]. Consequently, the electrochemical activity of $(La_{0.75-x}Sr_{0.25+x})_{0.95}Mn_{0.5}Cr_{0.5-x}Ti_xO_{3-\delta}$ can be expected to moderately decrease when x increases.

Oxygen permeation

Despite the small differences in the oxygen stoichiometry at elevated temperatures (inset of Fig. 3), the steady-state oxygen permeation fluxes (j) through dense $(La_{0.75-x}Sr_{0.25+x})_{0.95}Mn_{0.5}Cr_{0.5-x}Ti_xO_{3-\delta}$ membranes under a fixed oxygen pressure gradient and the corresponding activation energies are quite similar for all compositions (Fig. 12). This may suggest that the overall rate of oxygen transfer is determined by similar mechanisms, which are not directly related to the intrinsic factors, such as the oxygen vacancy concentration in the lattice bulk or metal-oxygen bonding strength dependent of the cation composition. The likely permeation-determining factors include, in particular, surface exchange kinetics and oxygen diffusion along the grain boundaries. In order to validate these assumptions, effects of the grain size on the steady-state oxygen permeation were assessed for $(La_{0.35}Sr_{0.65})_{0.95}Mn_{0.5}Cr_{0.1}Ti_{0.4}O_{3-\delta}$ ceramics sintered during 15 and 50 h (Figs. 12 and 13); their microstructures are compared in Fig. 2c, d. The results show that, indeed, decreasing the grain-boundary area causes a significant

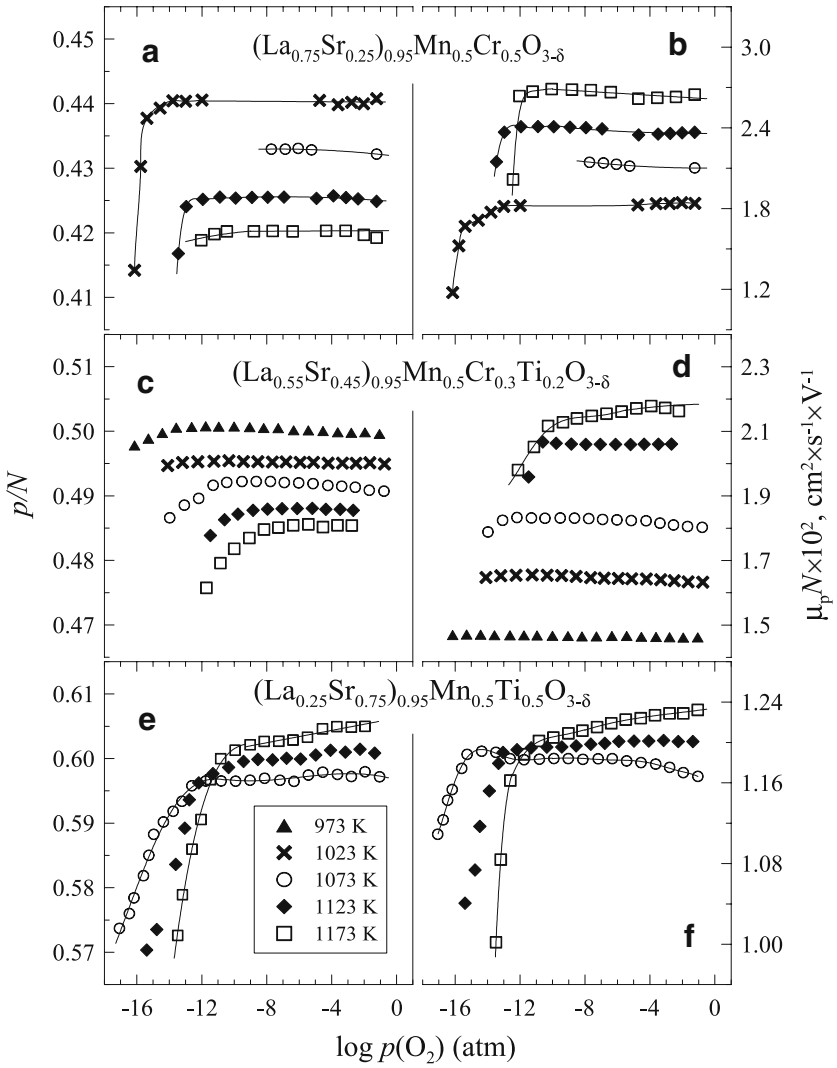

Fig. 10 Oxygen partial pressure dependencies of the p/N and $\mu_p \times N$ estimates for LSMCT0 (**a**, **b**), LSMCT2 (**c**, **d**), and LSMCT5 (**e**, **f**)

decrease in the oxygen fluxes, while the apparent activation energy remains essentially unchanged. The changes in the permeation fluxes are substantially larger than the level of experimental uncertainties and are well reproducible for the membranes with different thicknesses. The latter observation is illustrated by Fig. 13b, d, which compares the values of specific oxygen permeability $J(O_2)$ calculated as [15, 20]

$$J(O_2) = j \cdot d \cdot \left[\ln\left(\frac{p_2}{p_1}\right)\right]^{-1} \quad (3)$$

where p_1 is the oxygen partial pressure at the membrane permeate side, and d is the membrane thickness. It should also be mentioned that significant grain-boundary contributions to the oxygen ion diffusion are known for both $LaCrO_3$- and $LaMnO_3$-based materials with low oxygen nonstoichiometry [32–35]. The microstructural features associated with liquid phase-assisted sintering were reported to promote fast ionic conduction along the boundaries [33].

Further inspection of the results shown in Fig. 13 shows also a non-negligible role of the surface exchange kinetics. The specific oxygen permeability is proportional to $j \times d$, and should hence be thickness-independent when the exchange processes are fast [15, 20]. For $(La_{0.35}Sr_{0.65})_{0.95}Mn_{0.5}Cr_{0.1}Ti_{0.4}O_{3-\delta}$ membranes, increasing d leads to lower oxygen fluxes and higher $J(O_2)$ values due to a decreasing role of the interfacial exchange. This complex mechanism makes it impossible to unambiguously compare relative contributions of the grain bulk, grain boundaries, and surface to the overall membrane resistance to oxygen transfer. At the same time, one can note that the apparent ionic conductivity of $(La_{0.35}Sr_{0.65})_{0.95}Mn_{0.5}Cr_{0.1}Ti_{0.4}O_{3-\delta}$, roughly estimated from the permeation data using the model described in [20], is more than ten times higher than that of $La_{0.87}Sr_{0.13}Cr_{1.03}O_{3-\delta}$ ceramics [33] with an essentially grain-boundary transport. However, this level of oxygen ionic conduction is still insufficient to expect any considerable enhancement in the electrochemical reaction zone due to oxygen transport through electrode bulk, similar to $La(Sr)MnO_3$-based cathodes [36, 37].

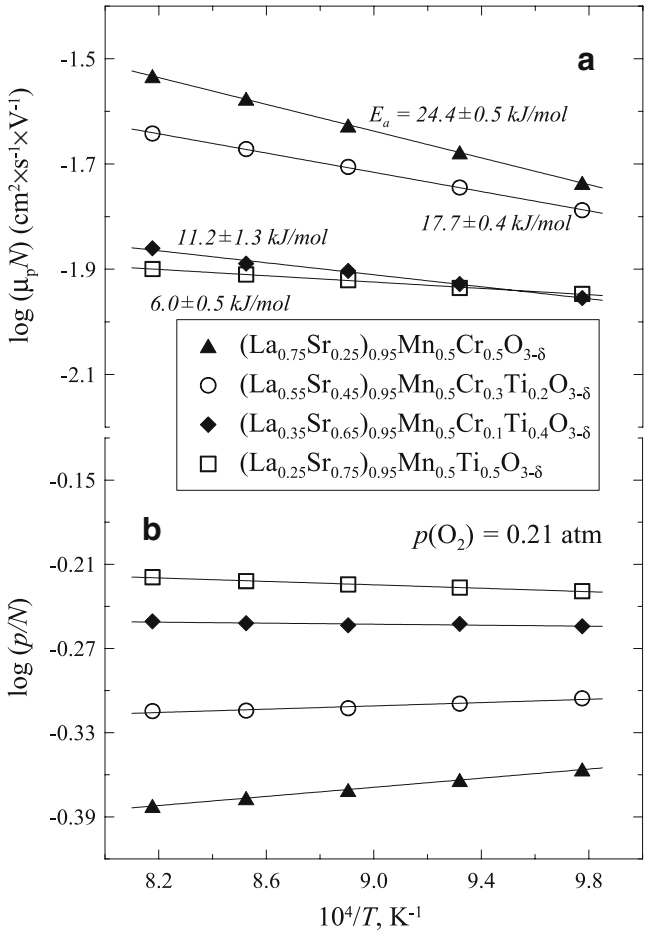

Fig. 11 Temperature dependencies of the estimated $\mu_p \times N$ (**a**) and p/N (**b**) values at atmospheric oxygen pressure

Electrode performance

Figures 14 and 15 illustrate the anodic behavior of $(La_{0.75-x}Sr_{0.25+x})_{0.95}Mn_{0.5}Cr_{0.5-x}Ti_xO_{3-\delta}$-based porous layers applied onto LSGM and $La_{10}Si_5AlO_{26.5}$ solid electrolytes in H_2-containing atmospheres. Typical examples of the impedance spectra are presented in Fig. 16. Increasing x in $(La_{0.75-x}Sr_{0.25+x})_{0.95}Mn_{0.5}Cr_{0.5-x}Ti_xO_{3-\delta}$ deteriorates the electrochemical activity of porous electrodes, while the effect of solid electrolyte is rather minor. Taking into account the significant difference in the transport and electrochemical properties of LSGM and $La_{10}Si_5AlO_{26.5}$ [19], these trends indicate that the rate-determining steps are related to the electrode surface or transport in the electrode bulk. Note that SEM/EDS studies showed no formation of blocking layers at the electrode/electrolyte interfaces (e.g., Fig. 2f). Although the diffusion of variable-valence cations into the electrolyte surface layers and surface poisoning of the electrodes applied onto $La_{10}Si_5AlO_{26.5}$ were observed by EDS, the latter factor cannot be considered as performance-limiting as the anodic overpotentials of LSGM- and $La_{10}Si_5AlO_{26.5}$-based half-cells are similar (Figs. 14 and 15). Furthermore, the relatively low and similar values of oxygen permeability of $(La_{0.75-x}Sr_{0.25+x})_{0.95}Mn_{0.5}Cr_{0.5-x}Ti_xO_{3-\delta}$ (Fig. 12) makes it impossible to correlate the electrochemical behavior and bulk ionic transport. The key factors may include, therefore, surface exchange kinetics and electronic conductivity.

The redox kinetics of $(La_{0.75}Sr_{0.25})_{0.95}Mn_{0.5}Cr_{0.5}O_{3-\delta}$ and $(La_{0.25}Sr_{0.75})_{0.95}Mn_{0.5}Ti_{0.5}O_{3-\delta}$ powders was compared analyzing their transient behavior on $p(O_2)$ variations, measured by TGA (Fig. 5). One example is presented in Fig. 17, which displays two weight relaxation curves and their analysis using the simple model

$$m(t) = m_1 + m_2 \exp\left(-\frac{t}{\tau}\right) \quad (4)$$

where m, t, and τ are the mass, time, and relaxation time constant, respectively. Note that the right term, $\exp(-t/\tau)$, is common for the description of non-steady-state diffusion and exchange processes and originates from solving the temporal part of the second Fick's law by separation of variables [38]. An exact agreement with Eq. 4 corresponds to substantial surface limitations, whereas the solutions for open and partly open boundaries (relatively fast surface exchange) may be represented by a series of exponential terms $\exp(-t/\tau_i)$ with τ_i calculated from the boundary

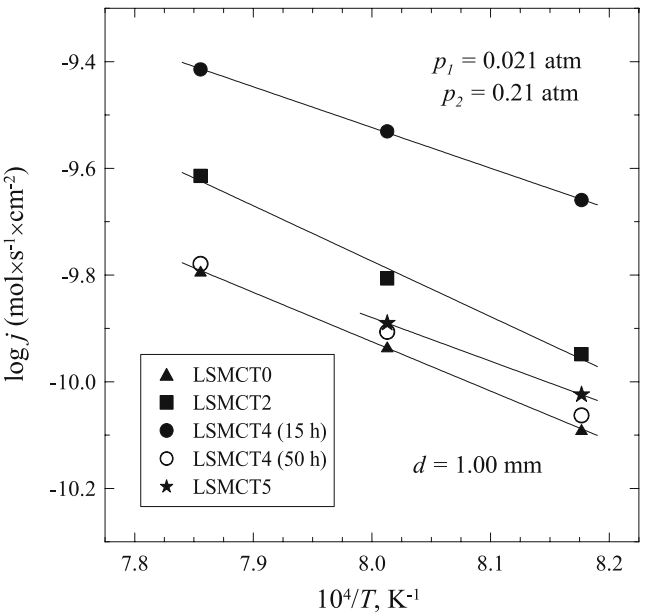

Fig. 12 Temperature dependencies of the oxygen permeation fluxes through dense $(La_{0.75-x}Sr_{0.25+x})_{0.95}Mn_{0.5}Cr_{0.5-x}Ti_xO_{3-\delta}$membranes under a fixed $p(O_2)$ gradient. For LSMCT4, the data on ceramics sintered during 15 and 50 h are compared. For other materials, the sintering time is 15 h. The membrane thickness is 1.00±0.02 mm

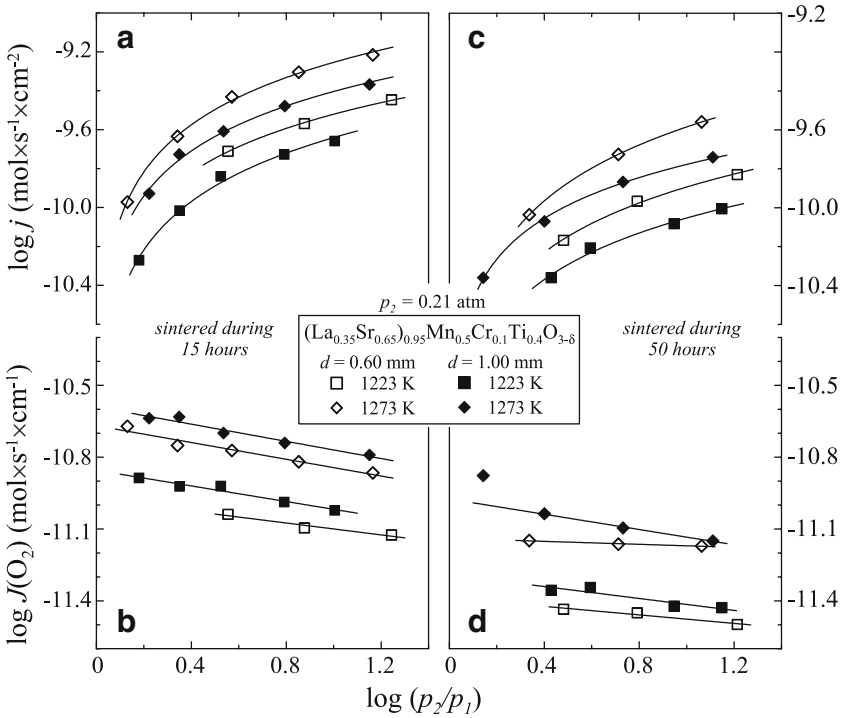

Fig. 13 Oxygen permeation fluxes (**a**, **c**) and specific permeability (**b**, **d**) of LSMCT4 membranes with various thicknesses, sintered during 15 h (**a**, **b**) and 50 h (**c**, **d**)

conditions and transport coefficients [38]. This model may be transformed into

$$\frac{m(t\to\infty)-m(t)}{m(t\to\infty)-m(t=0)}=\exp\left(-\frac{t}{\tau}\right) \tag{5}$$

and

$$\int_0^\infty \exp\left(-\frac{t}{\tau}\right)dt=\tau \tag{6}$$

which can be used to calculate τ by numerical integration of the experimental data. Also, deviations from linearity of the $\frac{m(t\to\infty)-m(t)}{m(t\to\infty)-m(t=0)}$ vs. $\exp(-t/\tau)$ plots enable to identify processes where the number of rate-determining steps is higher than one. The latter situation is indeed observed for the title materials (inset of Fig. 17b), but the redox kinetics and time constants exhibited by $(La_{0.75}Sr_{0.25})_{0.95}Mn_{0.5}Cr_{0.5}O_{3-\delta}$and $(La_{0.25}Sr_{0.75})_{0.95}Mn_{0.5}Ti_{0.5}O_{3-\delta}$ powders are similar within the limits of experimental error. In combination with the oxygen permeation data, this suggests essentially similar exchange rates. Therefore, the decrease of electrochemical activity of $(La_{0.75-x}Sr_{0.25+x})_{0.95}Mn_{0.5}Cr_{0.5-x}Ti_xO_{3-\delta}$ anodes with increasing x (Figs. 14 and 15) can be associated with lowering electronic conductivity in reducing atmospheres (Figs. 6 and 7).

In all cases, the surface modification with CeO_2 and Ni lowers the anodic overpotentials (Fig. 15). Such an improvement results from several factors, namely an

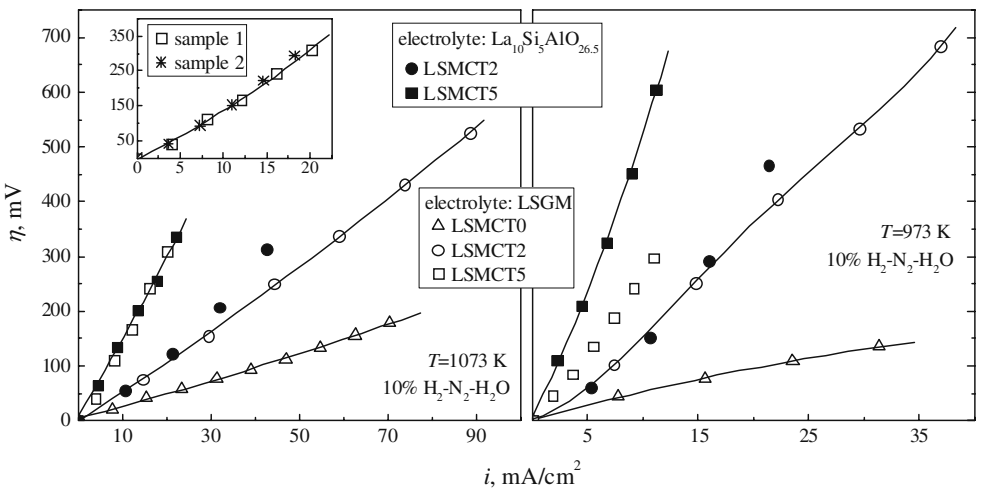

Fig. 14 Anodic overpotential vs. current density dependencies for as-prepared LSMCT0, LSMCT2, and LSMCT5 electrodes, applied onto LSGM and $La_{10}Si_5AlO_{26.5}$ solid electrolytes with CGO interlayer. The measurements were performed in humidified 10% H_2–90% N_2 flow at 973 and 1073 K. *Inset* shows one example of the reproducibility tests performed for two different samples of porous LSMCT5 deposited onto LSGM electrolyte

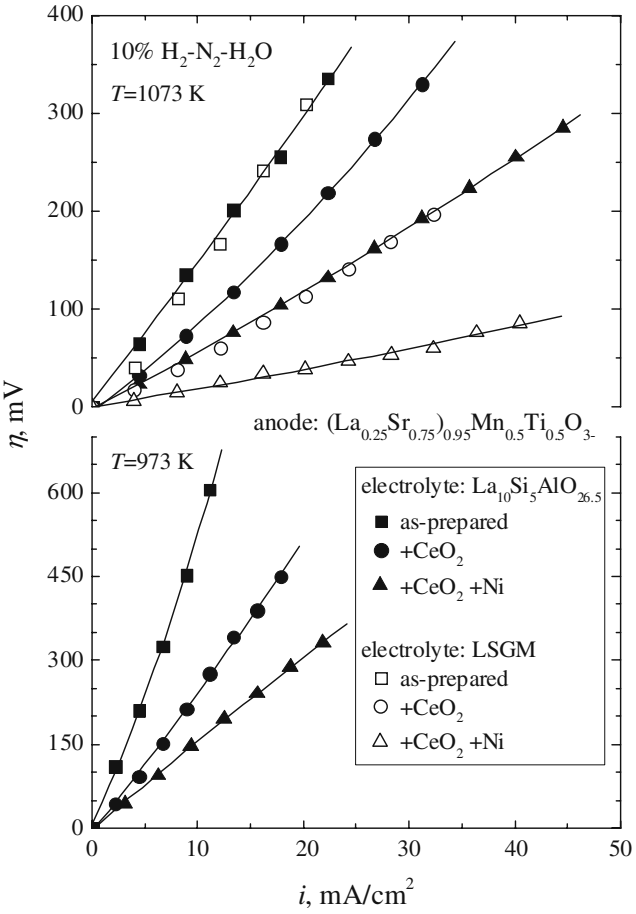

Fig. 15 Comparison of the anodic overpotentials for porous LSMCT5 porous electrodes after preparation and after infiltration of $CeO_{2-\delta}$ and Ni, in humidified 10% H_2–90% N_2 flow

increase in the triple-phase boundary length and electrode surface area, improved catalytic activity, and facilitated electronic transfer. After the infiltration of CeO_2 and Ni, the anodic overpotential of LSMCT5 | LSGM half-cell with CGO interlayer at 1073 K and current density of 40 mA/cm^2 decreases down to 85 mV (Fig. 15), i.e., down to the level comparable to the performance of Ti-free electrode without surface modification (Fig. 14). The positive impact of surface modification is more pronounced when the LSGM electrolyte is used, since the processes at the electrode/electrolyte and electrolyte/gas interfaces become critical for the overall electrode reaction rate when the electronic conduction in the electrode layer is improved. As a result, the performance of surface-modified anodes is generally better in contact with LSGM solid electrolyte compared to $La_{10}Si_5AlO_{26.5}$, in correlation with the oxygen-ionic and electronic conductivities of these electrolyte materials [19].

A qualitatively similar behavior was observed in oxidizing atmospheres where the conductivity of $(La_{0.75-x}Sr_{0.25+x})_{0.95}Mn_{0.5}Cr_{0.5-x}Ti_xO_{3-\delta}$ is much higher than in H_2-containing gas mixtures. In air, the electrode performance becomes strongly affected by the solid electrolyte material (Fig. 18) and is essentially independent of the perovskite phase composition at x=0–0.5, both under cathodic and anodic polarization (Fig. 19). These observations indicate that the rate-determining steps are related to the reaction zone in the vicinity of triple-phase boundary and/or at the electrode and electrolyte surfaces, while the role of the electrode electronic conductivity appears less significant. In the case of $La_{10}Si_5AlO_{26.5}$ electrolyte ceramics, the electrode overpotentials are much higher under cathodic than under anodic polarization; this trend is considerably less pronounced for the cells with LSGM solid electrolyte. Such a difference in the electrochemical behavior may partly originate from the incorporation of variable-valence cations into the electrolyte surface during the electrode preparation, confirmed by the EDS analysis in this and previous [15, 19] works. Anodic polarization raises the oxygen chemical potentials both in the electrode and interfacial electrolyte layers, locally increasing the oxygen-ion concentration and oxidation state of the variable-valence cations. For the oxygen-hyperstoichiometric silicates where the ionic transport is dominated by interstitial anions, the interfacial processes related to the oxygen

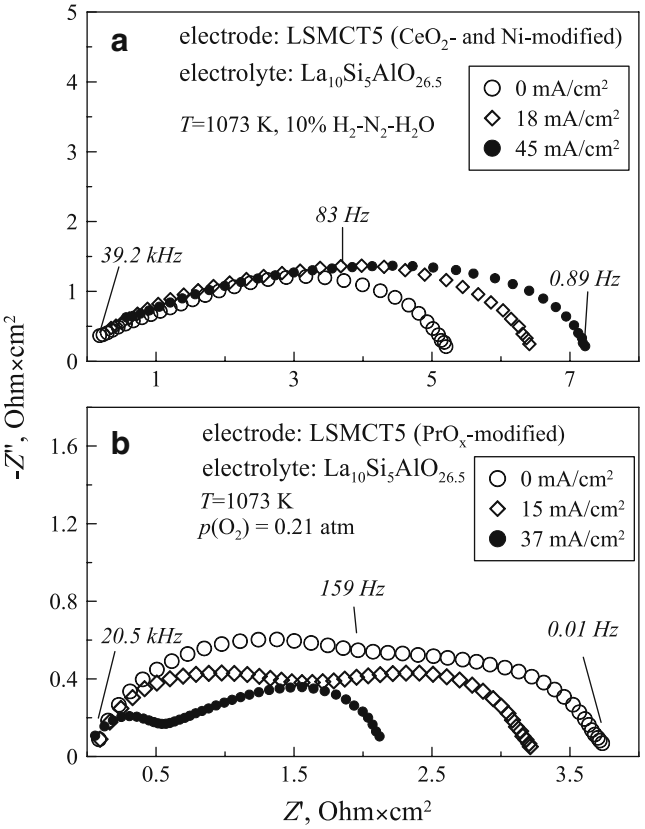

Fig. 16 Examples of typical impedance spectra corrected for the ohmic losses and normalized to the electrode surface area, in humidified 10% H_2–90% N_2 atm (**a**) and in air (**b**). Experimental conditions are given in the legends

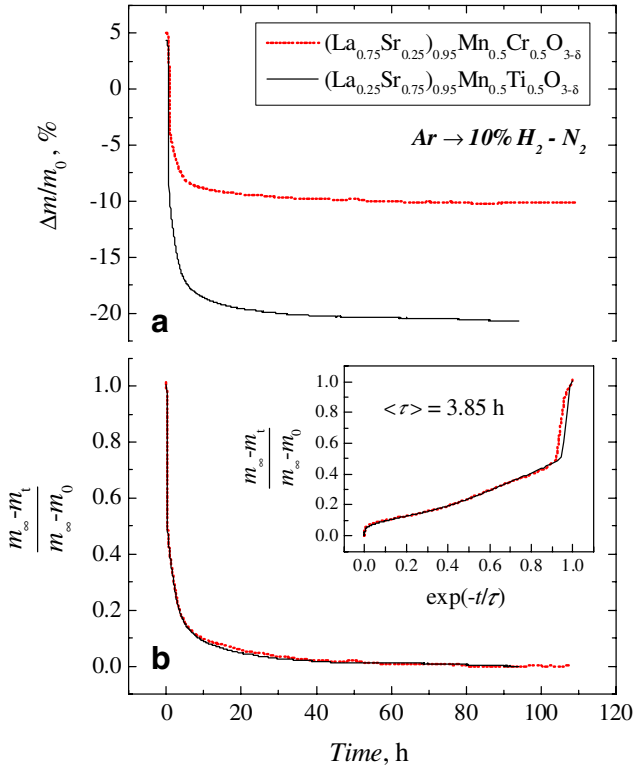

Fig. 17 Example of the relative weight changes of $(La_{0.75}Sr_{0.25})_{0.95}Mn_{0.5}Cr_{0.5}O_{3-\delta}$ and $(La_{0.25}Sr_{0.75})_{0.95}Mn_{0.5}Ti_{0.5}O_{3-\delta}$ powders on reduction after switching the atmosphere from flowing Ar to 10%H_2-N_2 at 1073 K (**a**), and reduction kinetics analysis (**b**). See text for details

transfer and diffusion should hence be facilitated under anodic polarization and hampered due to cathodic reduction. Increasing p-type electronic conduction at the electrolyte surface enriched with transition metal cations oxidized under anodic current in air should also result in a spatial expansion of the electrochemical reaction zone along the solid electrolyte, thus decreasing polarization resistance. This second factor is relevant for both $La_{10}Si_5AlO_{26.5}$ and LSGM electrolytes and explains well the influence of current direction on the overpotentials of electrodes in contact with oxygen-deficient lanthanum gallate-based electrolyte characterized by vacancy diffusion mechanism of ionic transport. As for most oxide electrodes [3, 15, 19], the overpotentials under oxidizing conditions can be drastically decreased by the infiltration of praseodymia, a result of enhanced exchange currents at both electrode/gas and electrolyte/gas interfaces. Nevertheless, the electrochemical activity of porous $(La_{0.75-x}Sr_{0.25+x})_{0.95}Mn_{0.5}Cr_{0.5-x}Ti_xO_{3-\delta}$ layers in air remains relatively low; for example, the cathodic overpotential of LSMCT5 | LSGM half-cell at 1073 K and current density of −80 mA/cm^2 is as high as −190 mV. Contrary to the anode behavior in reducing atmospheres, the polarization curves exhibit a Tafel-like behavior (Figs. 18 and 19); no tendencies to limiting currents are observed.

It should be separately noted that all the tested porous layers had similar microstructures, though no attempt to optimize the electrode morphology was made in the present work. The results showed a good reproducibility for different series of the samples, irrespective of the oxygen chemical potential in the gaseous phase (see inset in Figs. 14 and 18a). Also, no substantial alterations in the electrochemical behavior were observed after the current and temperature cycling; SEM inspections revealed no significant microstructural degradation after the measurements (Fig. 2e and f).

In summary, the results show that co-doping of $(La_{0.75}Sr_{0.25})_{0.95}Cr_{0.5}Mn_{0.5}O_{3-\delta}$ by Sr^{2+} and Ti^{4+} makes it possible to decrease chromium content down to zero without essential deteriorating effects on the transport properties and electrode performance under oxidizing conditions. The moderate increase of the thermal and chemical expansion, governed by the manganese cations

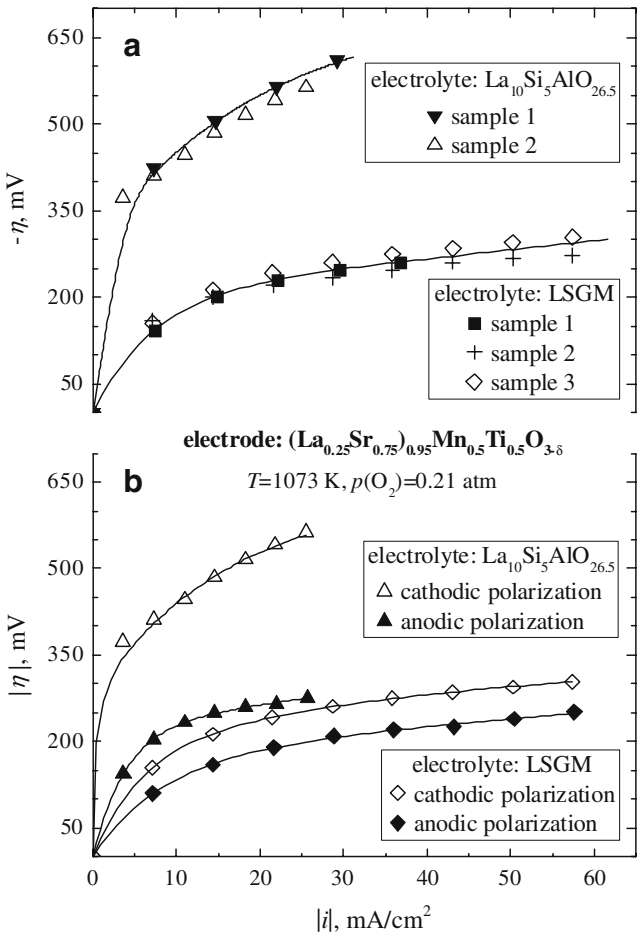

Fig. 18 Examples of the cathodic polarization curves of LSMCT5 electrodes in contact with LSGM and $La_{10}Si_5AlO_{26.5}$ solid electrolytes, illustrating reproducibility of the results obtained for different series of the porous electrode samples (**a**) and overpotential-current dependencies of LSMCT5 electrodes under cathodic and anodic polarization (**b**) in air at 1073 K

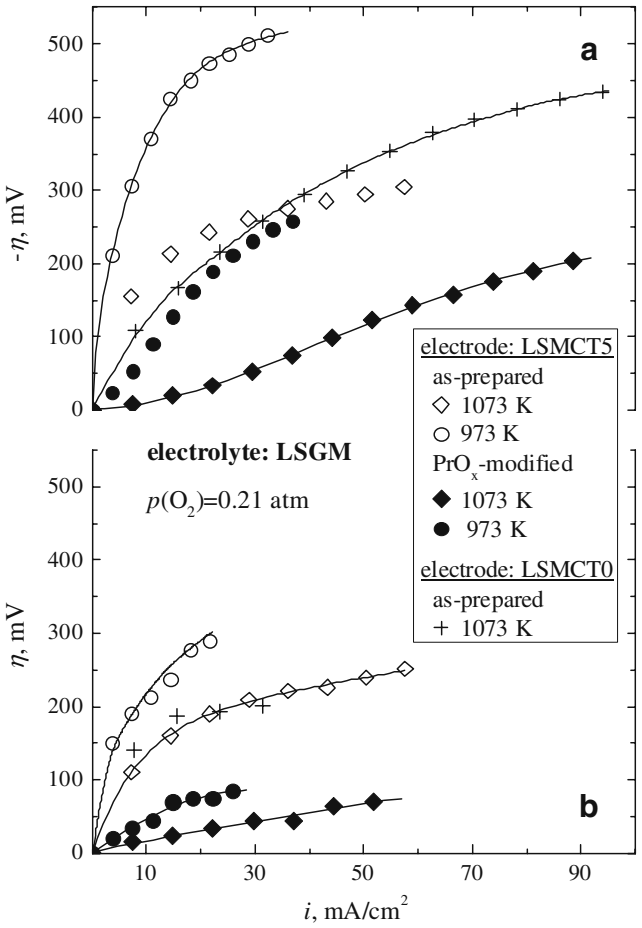

Fig. 19 Overpotential vs. current density dependences of as-prepared and PrO_x-modified $(La_{0.75-x}Sr_{0.25+x})_{0.95}Mn_{0.5}Cr_{0.5-x}Ti_xO_{3-\delta}$ electrodes in contact with LSGM electrolyte under cathodic and anodic polarization in air

in the B sublattice, may be suppressed by optimizing the acceptor/donor concentration ratio. The same factor, and minor additions of other transition metal cations such as Ni, can be used to increase electronic conductivity and electrochemical activity of the porous SOFC cathodes. However, aliovalent doping with acceptor- and donor-type cations may hardly be expected to suppress the conductivity drop at low $p(O_2)$, which is critical for the anode performance and makes it necessary to incorporate electronically conducting components in the porous electrodes operating in reducing atmospheres.

Acknowledgements This work was partially supported by the FCT, Portugal (projects PTDC/CTM/64357/2006, SFRH/BD/45227/2008, SFRH/BPD/28629/2006, and SFRH/BPD/28913/2006), by the European Commission (project STRP 033410-MatSILC), and by the Ministry of Education and Science of the Russian Federation (state contract 02.740.11.5214).

References

1. Fuel Cell Handbook (2004) EG&G technical services, 7th edn. Morgantown, West Virginia
2. Möbius H-H (1997) J Solid State Electrochem 1:2
3. Tsipis EV, Kharton VV (2008) J Solid State Electrochem 12:1367
4. Gorte RJ, Park S, Vohs JM, Wang C (2000) Adv Mater 12:1465
5. Tsipis EV, Kharton VV, Frade JR (2005) J Eur Ceram Soc 25:2623
6. Marina OA, Canfield NL, Stevenson JW (2002) Solid State Ionics 149:21
7. Canales-Vásques J, Tao SW, Irvine JTS (2003) Solid State Ionics 159:159
8. Primdahl S, Hansen JR, Grahl-Madsen L, Larsen PH (2001) J Electrochem Soc 148:A74
9. Tao S, Irvine JTS (2004) J Electrochem Soc 151:A252
10. Zha S, Tsang P, Cheng Z, Liu M (2005) J Solid State Chem 178:1844
11. Ruiz-Moralez JC, Canales-Vazquez J, Peña-Martínez J, Marrero-López D, Núñez P (2006) Electrochim Acta 52:278
12. Lu XC, Zhu JH (2007) Solid State Ionics 178:1467
13. Chen XJ, Liu QL, Khor KA, Chan SH (2007) J Power Sources 165:34
14. Wan J, Zhu JH, Goodenough JB (2006) Solid State Ionics 177:1211
15. Kharton VV, Tsipis EV, Marozau IP, Viskup AP, Frade JR, Irvine JTS (2007) Solid State Ionics 178:101
16. Jiang SP, Zhang L, Zhang Y (2007) J Mater Chem 17:2627
17. Shaula AL, Kharton VV, Marques FMB (2005) J Solid State Chem 178:2050
18. Kharton VV, Shaula AL, Vyshatko NP, Marques FMB (2003) Electrochim Acta 48:1817
19. Tsipis EV, Kharton VV, Frade JR (2007) Electrochim Acta 52:4428
20. Marozau IP, Kharton VV, Viskup AP, Frade JR, Samakhval VV (2006) J Eur Ceram Soc 26:1371
21. Plint SM, Connor PA, Tao S, Irvine JTS (2006) Solid State Ionics 177:2005
22. Oishi M, Yashiro K, Sato K, Mizusaki J, Kawada T (2008) J Solid State Chem 181:3177
23. Tsipis EV, Kharton VV (2008) J Solid State Electrochem 12:1039
24. Okamura T, Shimizu S, Nogi M, Tanimura M, Furuya K, Munakata F (2004) J Power Sources 130:38
25. Mizusaki J (1992) Solid State Ionics 52:79
26. Anderson HU, Kuo JH, Sparlin DM (1989) In: Singhal SC (ed) SOFC I. The Electrochemical Society, Pennington, p 111, PV89-11
27. Hahn WC Jr, Muan A (1960) Am J Sci 258:66
28. Nakamura T, Petzow G, Gauckler LJ (1979) Mater Res Bull 14:649
29. Yasuda I, Hishinuma M (1996) J Solid State Chem 123:382
30. Kofstad P (1972) Nonstoichiometry, diffusion and electrical conductivity in binary metal oxides. Wiley, New York
31. Raffaelle R, Anderson HU, Sparlin DM, Parris PE (1991) Phys Rev B 43:7991
32. Kawada T, Horita T, Sakai N, Yokokawa H, Dokiya M (1995) Solid State Ionics 79:201
33. Suzuki M, Sasaki H, Kajimura A (1997) Solid State Ionics 96:83
34. Lee DK, Yoo HI (2000) J Electrochem Soc 147:2835
35. Berenov AV, MacManus-Driscoll JL, Kilner JA (1999) Solid State Ionics 122:41
36. Jiang SP (2002) Solid State Ionics 146:1
37. Takeda Y, Kanno R, Noda M, Tomida Y, Yamamoto O (1987) ci 134:2656
38. Crank J (1975) The mathematics of diffusion, 2nd edn. Oxford Univ Press, Oxford